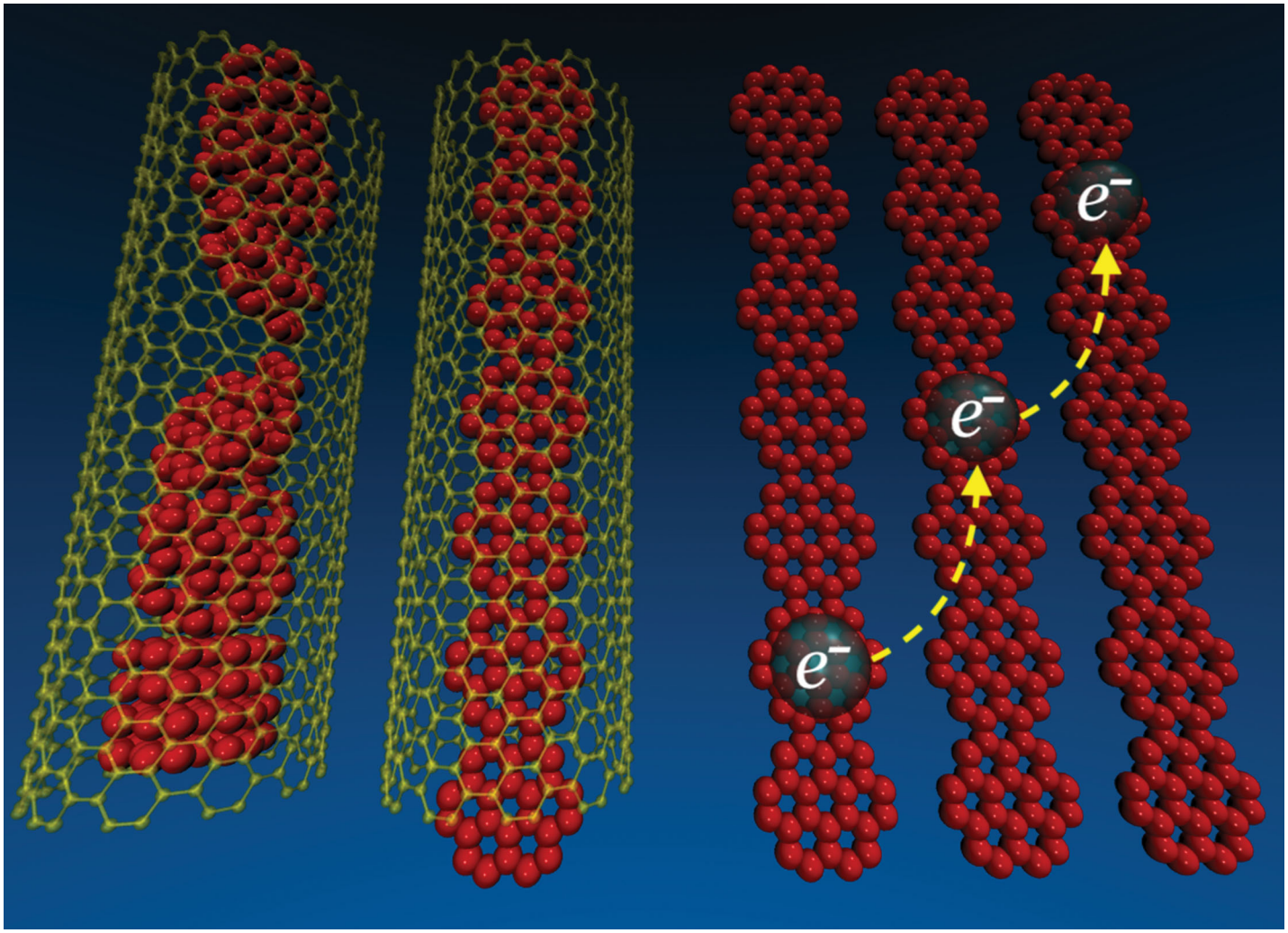

Showcasing research from University of Brasília, Brazil.

Transport of quasiparticles in coronene-based graphene nanoribbons

The synthesis of coronene-based graphene nanoribbons occurs within a carbon nanotube as an ideal environment. The charge transport mechanism in this novel graphene-like lattice is mediated by polarons and bipolarons.

As featured in:

See Luiz Antônio Ribeiro Júnior *et al.*, *J. Mater. Chem. C*, 2020, **8**, 12100.

ROYAL SOCIETY OF CHEMISTRY

rsc.li/materials-c

Registered charity number: 207890

Journal of Materials Chemistry C

ROYAL SOCIETY OF CHEMISTRY

PAPER

Published on 28 May 2020
Licence and permissions

Cite this: J. Mater. Chem. C, 2020, 8, 12100

Transport of quasiparticles in coronene-based graphene nanoribbons

Marcelo Lopes Pereira Júnior,[a] Bernhard Georg Enders Neto,[b] William Ferreira Giozza,[c] Rafael Timóteo Sousa Júnior,[c] Geraldo Magela e Silva[a] and Luiz Antônio Ribeiro Júnior *[ab]

Received 13th March 2020,
Accepted 28th May 2020

DOI: 10.1039/d0tc01319f

rsc.li/materials-c

Inspired by accomplishments of graphene in nanoelectronics, several carbon allotropes were proposed recently. Computational and experimental studies have been performed to describe their fundamental features toward improvement in applications regarding energy conversion and storage. However, investigations about crucial aspects behind the material's performance, such as the formation and dynamics of charge carriers, are missing for several of those allotropes so far. Here, we numerically investigate the stability and transport properties of polarons and bipolarons in coronene-based graphene nanoribbons (CNRs), which were recently synthesized. A 2D tight-binding Hamiltonian endowed with lattice relaxation effects is developed to describe the formation of these quasiparticle species. A semi-classical transport approach is used to study the stationary and dynamical properties of charge carriers in the presence of an external electric field. Remarkably, the results reveal that polaron and bipolaron formation takes place in both armchair and zigzag CNRs but, only in the former, these quasiparticles are mobile. The mobility of polarons is considerably higher than that of bipolarons, once the latter have larger effective mass. In contrast, bipolarons are more stable and support electrical field strengths of higher intensity than polarons.

1 Introduction

Since the discovery of conducting molecular crystals in the 60s,[1–3] organic compounds have been studied to propose new routes for developing optoelectronic devices with good cost-efficiency compromise aiming at revolutionizing green energy solutions.[4,5] Different organic materials can be used in the manufacturing process of these devices, ranging from one-dimensional systems with covalent bonds (polymers)[6] to three-dimensional lattices of small molecules with van der Waals type interactions (molecular crystals),[7] which have very distinct structural and electronic properties. Among these carbon-based materials, graphene and its allotropes attract priority attention due to their attractive mechanical, electronic, and optical properties.[8–10] Coronene, a large polycyclic aromatic hydrocarbon molecule in which electrons are delocalized among six perifused benzene rings,[11] can be encapsulated in carbon nanotubes to obtain a graphene allotrope, namely coronene-based graphene nanoribbons (CNRs).[12,13] In this process, two types of endings can be obtained: armchair and zigzag. Importantly, both types of cutting edges have already been synthesized.[12,13] Regardless of the purpose, charge transport is a crucial aspect that should be deeply studied prior to usage of these materials.

When it comes to organic semiconductors, the most common charge carrier is the polaron, which is a quasiparticle formed from the interaction between excess charge (electron or hole) and local lattice deformations.[14,15] Bipolarons, in turn, can be generated by recombination of two polarons with the same charge and antiparallel spins.[14,15] In this sense, polarons have spin $\pm 1/2$ and charge $\pm e$, while bipolarons are spinless structures with charge $\pm 2e$.[2] The formation of both species of quasiparticles was experimentally[16] or theoretically[17–22] reported for the case of armchair graphene nanoribbons. Much effort has been employed in studying the charge transport in standard graphene nanoribbons from the theoretical point of view.[19,20,22–28] A quantum transport algorithm, based on the nonequilibrium Green function formalism combined with density-functional theory (NEGF-DFT), was developed to simulate conductance in devices based on graphene nanoribbons involving a large number of atoms.[24] Importantly, these full DFT calculations cannot tackle lattice relaxation effects. In this sense, to realize the dynamics of polarons and bipolarons in graphene-based nanoribbons, an approach that includes lattice relaxation dynamics should be considered.

[a] Institute of Physics, University of Brasília, 70.919-970, Brasília, Brazil. E-mail: ribeiro.jr@unb.br
[b] PPGCIMA, Campus Planaltina, University of Brasília, 73.345-010, Brasília, Brazil
[c] Department of Electrical Engineering, University of Brasília, 70.919-970, Brasília, Brazil

Recently, experimental and theoretical studies have presented the synthesis, structural, and electronic properties of CNRs with usual armchair (ACNR) and zig-zag (ZCNR) bordering.[12,13] As mentioned above, CNRs can be synthesized from the confinement of coronene molecules in carbon nanotubes. This process facilitates the alignment of end-to-end molecules, which makes possible the dimerization and oligomerization of molecules in long nanoribbons. The electronic structure of ACNRs and ZCNRs was theoretically studied using density functional theory calculations to relate the features of a coronene molecule and the resulting CNRs.[29] The results indicate several magnetic states for the nanoribbon case and dependence of the electronic bandgap regarding both the number of atoms in the structure and electronic spin configuration. Although the relevant studies mentioned above have described some essential characteristics of CNRs, the charge transport mechanism in these materials remains not investigated. In this sense, the present study fills this gap by providing a deep understanding of the stability and dynamics of polarons and bipolarons in CNRs.

Herein, we investigate the charge transport mechanism in CNRs by employing a 2D tight-binding model Hamiltonian that takes into account lattice relaxation effects. In particular, the stationary and dynamical properties of polarons and bipolarons in CNRs are the specific issues tackled by the present work. Our computational protocol is based on a semi-empirical set of parameters obtained to describe the transport of these quasiparticles in CNRs. Notably, the results suggest that both polarons and bipolarons assist the charge transport mechanism in armchair CNRs. On the other hand, in zig-zag CNRs, these quasiparticles are formed, but no charge transport takes place.

2 Methodology

The formation and transport mechanisms of polarons and bipolarons in ACNR and ZCNR lattices (see Fig. 1) are studied here by using a 2D tight-binding model Hamiltonian developed to account the electronic (quantum) and lattice (classical) contributions simultaneously. Importantly, CNRs have fixed widths limited by the coronene molecule width that is used to form them. In this sense, our approach consists of a modified version of the Su–Schrieffer–Heeger Hamiltonian[30,31] that has the following form:

$$H = -\sum_{\langle i,j\rangle,s}\left(t_{i,j}C_{i,s}^{\dagger}C_{j,s} + t_{j,i}^{*}C_{j,i}^{\dagger}C_{i,s}\right) + \frac{1}{2}K\sum_{\langle i,j\rangle}\eta_{i,j}^{2} + \frac{1}{2M}\sum_{i}p_{i}^{2}. \quad (1)$$

since the position of atoms in CNRs is not substantially altered, the Hückel approximation ensures that electronic transfer integrals for π-electrons between nearest-neighboring sites ($t_{i,j}$) can be expanded to the first order. In this sense,

$$t_{i,j} = t_0 - \alpha\eta_{i,j} \quad (2)$$

where t_0 is the transfer integral for a lattice with equally spaced atoms, α represents the electron–phonon coupling constant

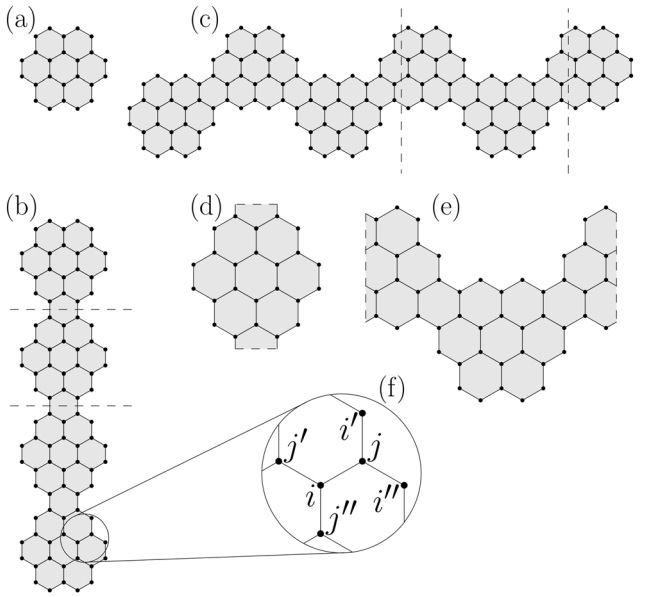

Fig. 1 Schematic representation of (a) coronene structure; (b) armchair coronene nanoribbon (ACNR); (c) zigzag coronene nanoribbon (ZCNR); (d) unit cells of ACNR; (e) unit cells of ZCNR; and (f) indices in CNRs.

that couples the two distinct degrees of freedom, and $\eta_{i,j}$ are the variations of the bond-lengths of two neighboring sites i and j.

In the first part of eqn (1) (electronic term), $\langle i,j\rangle$ represents the indexes of neighboring sites (see Fig. 1(e)), $C_{i,s}$ is the annihilation operator of a π-electron of an i site and with spin s, and $C_{j,s}^{\dagger}$ represents the corresponding creation operator of a j site. The second term is the effective potential associated with σ-bonds between carbon atoms, considered from a harmonic approximation, with K being the elastic constant associated with this approximation. The last term describes the kinetic energy of the sites in terms of their momenta p_i, where M is the mass of the site.

Starting from an initial random set of coordinates $\{\eta_{i,j}\}$, the stationary solution of the system, with $p_i = 0$ (static), can be found as follows. A self-consistent ground state is obtained from the diagonalization of the electronic Hamiltonian, according to the expression

$$H = -\sum_{k} E_{k,s}a_{k,s}^{\dagger}a_{k,s}, \quad (3)$$

where E_k are the energy eigenvalues of the electronic system. To do this procedure, it is necessary to obtain the operator a_k, which enables a diagonal Hamiltonian. These operators are obtained from a LCAO to determine the creation and annihilation operators:

$$a_{k,s} = \sum_{i}\psi_{k,i,s}C_{i,s}. \quad (4)$$

From these considerations, the electronic Hamiltonian becomes

$$H = -\sum_{\langle i,j\rangle,s,k,k'}\left(t_{i,j}\psi_{k,i,s}\psi_{k',j,s}^{*} + t_{i,j}^{*}\psi_{k,j,s}\psi_{k',i,s}^{*}\right)a_{k,s}^{\dagger}a_{k',s}, \quad (5)$$

which is diagonalized as long as the condition

$$-t_{i,j}\psi_{k,j,s} - t_{i,j'}\psi_{k,j',s} - t_{i,j''}\psi_{k,j'',s} = E_k\psi_{k,i,s} \quad (6)$$

holds for neighboring sites i, j, l, and m (see Fig. 1(e)).

The lattice solution is classically obtained from the solution of the Euler–Lagrange equations:

$$\frac{\mathrm{d}}{\mathrm{d}t}\left(\frac{\partial\langle L\rangle}{\partial\dot{\xi}_i}\right) - \frac{\partial\langle L\rangle}{\partial\xi_i} = 0. \quad (7)$$

Therefore, to take into account the lattice effects, it is necessary to obtain the expectation value of the Lagrangean, $\langle\psi|L|\psi\rangle$, where $|\psi\rangle$ is the Slater wave function represented in the second quantization formalism by $|\psi\rangle = |a_1^{\dagger}a_2^{\dagger}\ldots a_n^{\dagger}\rangle$. The Lagrangean is,

$$L = \frac{M}{2}\sum_i \dot{\xi}_i^2 - \frac{1}{2}K\sum_{\langle i,j\rangle}\eta_{i,j}^2 + \sum_{\langle i,j\rangle,s}\left(t_0 - \alpha\eta_{i,j}\right)\left(C_{i,s}^{\dagger}C_{j,s} + C_{j,s}^{\dagger}C_{i,s}\right) \quad (8)$$

thus,

$$\langle L\rangle = \frac{M}{2}\sum_i \dot{\xi}_i^2 - \frac{1}{2}K\sum_{\langle i,j\rangle}\eta_{i,j}^2 + \sum_{\langle i,j\rangle,s}\left(t_0 - \alpha\eta_{i,j}\right)B_{i,j}, \quad (9)$$

where

$$B_{i,j} \equiv {\sum_{k,s}}'\psi_{k,s}^{*}(i,t)\psi_{k,s}(j,t), \quad (10)$$

and ξ_i are the coordinates for a given site. The sum is realized only for the occupied states. It is noted also that the last equation is responsible for the connection between the electronic and lattice parts of the system.

An initial set of lattice coordinates ($\{\eta_{i,j}\}$) is used to perform a self-consistent calculation for obtaining a corresponding set $\{\psi_{k,i}\}$, which when solved returns a new set of coordinates $\{\eta_{i,j}\}$ until achieving a given convergence criterion. From the stationary solution $\{\eta_{i,j}\}$ and $\{\psi_{k,i}\}$, the time evolution of the system is performed by solving the time-dependent Schrödinger equation for electron dynamics along with the Euler–Lagrange equation for the movement of the atoms in the lattice. Thus, the electronic part of the system is described by

$$i\hbar\frac{\partial|\psi_k(t)\rangle}{\partial t} = H|\psi_k(t)\rangle, \quad (11)$$

with the evolution over time being given by

$$|\psi_k(t+\mathrm{d}t)\rangle = \mathrm{e}^{-\frac{i}{\hbar}H(t)\mathrm{d}t}|\psi_k(t)\rangle. \quad (12)$$

Now, expanding the wave function $|\psi_k(t)\rangle$ in a basis of eigenstates of the electronic Hamiltonian at time t, we obtain

$$|\psi_k\rangle = \sum_l D_{k,l}|\phi_l(t)\rangle. \quad (13)$$

Finally, we obtain the temporal evolution of the electronic part of the system, according to the final expression

$$|\psi_k(t+\mathrm{d}t)\rangle = \sum_l\langle\phi_l(t)|\psi_k(t)\rangle\mathrm{e}^{-\frac{i}{\hbar}\varepsilon_l\mathrm{d}t}|\phi_l(t)\rangle, \quad (14)$$

where $|\phi_l\rangle$ and $\{\varepsilon_l\}$ are the eigenkets and the eigenvalues of the electronic Hamiltonian at time t, respectively.

For the classical treatment governing the lattice part of the system, the solution of the coupled electronic part and the complete Euler–Lagrange equations are required as well. Its solution can be written as a Newtonian equation able to describe the movement of the sites in the system and is given by $F_{i,j}(t) = M\ddot{\eta}_{i,j}$, where

$$M\ddot{\eta}_{i,j} = \frac{1}{2}K\left(\eta_{i,j'} + \eta_{j'',i} + \eta_{j,i'} + \eta_{i'',j}\right) - 2K\eta_{i,j} \quad (15)$$

$$+\frac{1}{2}\alpha\left(B_{i,j'} + B_{j'',i} + B_{j,i'} + B_{i'',j} - 4B_{i,j} + \mathrm{C.C.}\right). \quad (16)$$

To simulate the quasiparticle dynamics in the system, an external electric field, $E(t)$, was included in our model by means of a time-dependent vector potential, $A(t)$, using a Peierls substitution for the phase factor of the electronic transfer integral

$$t_{i,j} = \exp(-i\gamma\mathrm{A}) \times (t_0 - \alpha\eta_{i,j}) \quad (17)$$

where $\gamma \equiv ea/(\hbar c)$, with a being the lattice parameter, e being the absolute value of the electronic charge, and c representing the speed of light. The relationship between the time-dependent electric field and the potential vector is given by $E(t) = -(1/c)\frac{\mathrm{d}A(t)}{\mathrm{d}t}$. In our model, the electric field is triggered adiabatically, according to the following expressions

$$A(t) = \begin{cases} 0 & \text{if } t < 0, \\ -\frac{1}{2}E\left(t - \frac{\tau}{\pi}\sin\left(\frac{\pi t}{\tau}\right)\right) & \text{if } 0 \le t < \tau, \\ -E\left(t - \frac{\tau}{2}\right) & \text{if } \tau \le t. \end{cases} \quad (18)$$

Here, E is the intensity of the electric field, and τ is the instant in which the electric field reaches its maximum intensity. The electric field is adiabatically activated to avoid numerical oscillations inserted in the lattice that appears when the electric field is turned on abruptly. In our simulations, the set of parameters used is based on other theoretical and experimental studies with the following values: t_0 = 2.7 eV, K = 21 eV Å^{-1}, a = 1.42 Å, and M = 12 u.[23,26,27,32,33] The electron–phonon coupling (α) varies between 2.0 and 6.0 eV Å^{-1}, while the external electric field intensity E_0 varies from 0.2 to 1.0 mV Å^{-1}.

3 Results and discussion

We begin our discussions by showing the numerical protocol used to determine the electron–phonon coupling strength of CNRs. This parameter is fundamental to study the formation and dynamics of quasiparticles in these materials. Fig. 2 shows the ACNR (blue curve) and ZNRS (red curve) bandgaps for α strengths varying from 2–6 eV Å^{-1}, considering neutral lattices. For the sake of comparison, this figure also depicts the bandgaps for the standard armchair graphene nanoribbon with seven atoms width (black curve in Fig. 2). This particular nanoribbon has a similar width when compared with an ACNR

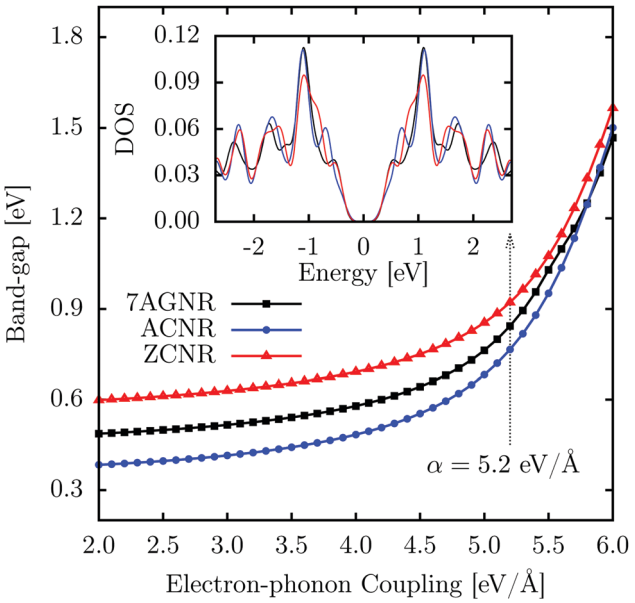

Fig. 2 Bandgap as a function of the electron–phonon coupling (α) for the model nanoribbons studied here. In this figure, just the neutral cases are shown. The inset depicts the density of states (DOS) for ACNR (blue), ZCNR (red), and 7AGNR (black) systems with α = 5.2 eV Å^{-1}.

lattice, which also possesses seven atoms of ending. These bandgaps are inferred from the density of states (DOS) plots, as illustrates by the inset panel of Fig. 2 for the α = 5.2 eV Å^{-1} case. In carbon-based materials, the degree of lattice distortion can be correlated with the bandgap opening in the sense that the narrower this opening is, the stiffer the lattice. Consequently, the weaker the coupling between the charge and lattice. It also means that in narrower bandgap organic systems, polarons/bipolarons tend to be unstable structures until they reach a critical limit in which the optoelectronic processes are mediated only by free electrons or holes. In light of these arguments, we can conclude that ZCNRs are less stiff lattices and present higher possibility of forming stable quasiparticles since they have higher bandgap values, as illustrated in Fig. 2. We can also infer that ACNRs are the lattices with a lower degree of distortion. Even so, stable polarons and bipolarons can be formed in these lattices, as shown later. Interestingly, the 7AGNR case defines a critical bandgap that marks the transition from ACNR towards ZCNR symmetry for a particular α strength. α = 6.0 eV Å^{-1} represents a threshold where, above it, the model lattices present the same degree of stiffness and favorable energetic framework to form stable polarons and bipolarons. It is worthwhile to mention that a CNR lattice with α = 5.2 eV Å^{-1} reproduces the bandgap values found in the literature.[12,13] For that reason, we have fixed this coupling strength for all the dynamics calculations performed here.

Once all the necessary parameters are settled, we now discuss the formation of charge carriers in CNRs. Fig. 3 shows

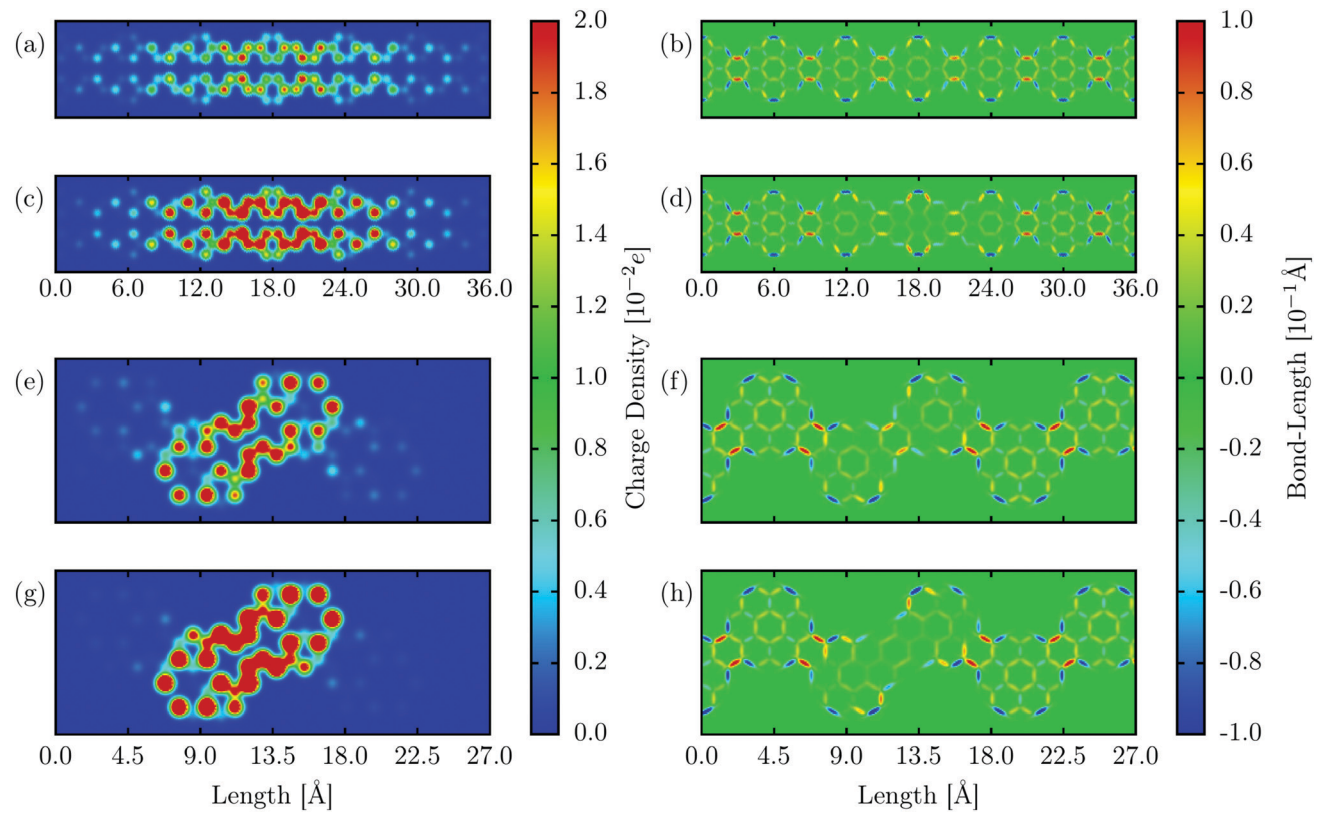

Fig. 3 Stationary solutions for charge density (CD) and bond-length (BL) configurations of CNR lattices containing a polaron and a bipolaron. Panels (a and b), (c and d), (e and f), and (g and h) present, respectively, the CD and BL signatures for a polaron in ACNR, a bipolaron in ACNR, a polaron in ZCNR, and a bipolaron in ZCNR.

the stationary solutions for the bond-length (Fig. 3(a) and (c)) and mean charge density (Fig. 3(b) and (d)) profiles considering an ACNR lattice that contains a polaron (top panels) or a bipolaron (bottom panels). The whole model CNR molecules simulated here have a length of 250 Å. To better visualize the results, the panels in Fig. 3 present a portion of the lattice near the region where the charge carrier is localized. For the rest of the lattice, the bond-length and charge density profiles are similar to the regions without charge. The polaron is formed by adding/removing an electron to/from the lattice, whereas the same process involving two electrons yields a bipolaron. As a consequence, the lattice is locally polarized in the region where the extra charge is located, yielding local deformations. In this sense, polarons and bipolarons are composite quasiparticles in which the extra charge is spatially localized and surrounded by phonons. This concept manifests itself in the results presented in Fig. 3. For both polaron and bipolaron cases, one can note that extra charge is symmetrically distributed along the nanoribbon length. The additional electron that forms the polaron is almost totally localized in three coronene-cells (red, green, and yellow spots), having one of these cells as a central unit, as shown in Fig. 3(a). The lattice containing a bipolaron presents a similar trend for the charge localization pattern. However, since two electrons form the bipolaron, the red regions are much more pronounced than in the polaron case. These charge localization signatures affect the lattice by causing changes in the bond-lengths locally, diminishing their distortions, as depicted in Fig. 3(b) and (d). Such a change in bond-length can be noticed by the weakening of colors, towards green, in the center of the cells that contain an extra charge. The bond-lengths suffer higher deviations for the bipolaron case when compared to the polaron one, due to the additional electron. Similar results are obtained for the polaron and bipolaron formation in ZCNRs, as shown in Fig. 3(e)–(h). Due to the way of cutting, these charge carriers are more localized in ZCNRs than ACNRs. In the former, the net charge is symmetrically distributed in two coronene-cells showing only red spots due to a higher confinement degree of the charge carrier. Note that in standard zigzag graphene nanoribbons, the net charge is spread over the ribbon borders giving rise only to edge states with free-like electrons.[34] Remarkably, ZCNRs can represent an advance for applications in which the generation of polarons and bipolarons plays an important role. Importantly, both quasiparticles are dynamically stable in the presence of an external electric field in ACNRs. Despite polarons and bipolarons being formed in ZCNRs, it is well known that they are not mobile in zig-zag graphene nanoribbons and their derivatives.[34] In this sense, the dynamical behavior of these charge carriers is discussed below only for ACNR lattices.

The polaron and bipolaron dynamics in the presence of an external electric field for ACNR lattices is illustrated in Fig. 4. This figure shows the temporal evolution of the mean charge density of a polaron (Fig. 4(a)) and a bipolaron (Fig. 4(b)) for a field strength of 0.8 mV Å^{-1}, during 215 fs. In these figures, each frame corresponds to a distinct period. After a transient time of acceleration, both carriers present linear displacement reaching saturation velocities of 0.38 Å fs^{-1} and 0.19 Å fs^{-1} for the polaron and bipolaron cases, respectively. Since the bipolaron's effective mass is higher than the polaron one, it tends to present smaller final velocities for a given field strength. It is worthwhile to stress that these velocities are substantially

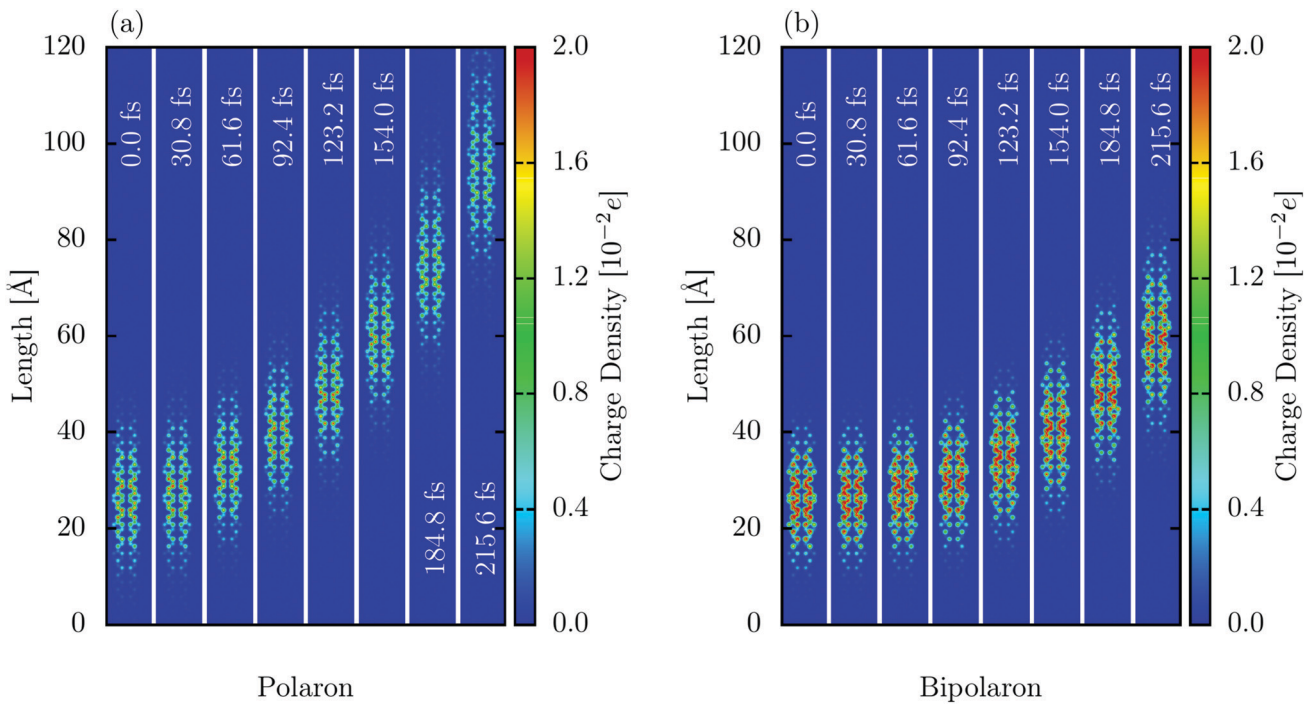

Fig. 4 Time evolution of atomic charge density for a polaron (left) and a bipolaron (right) in an ACNR lattice for an electric field strength of E_0 = 0.8 mV Å^{-1}. Each frame in these panels denotes a different period, which is highlighted within it.

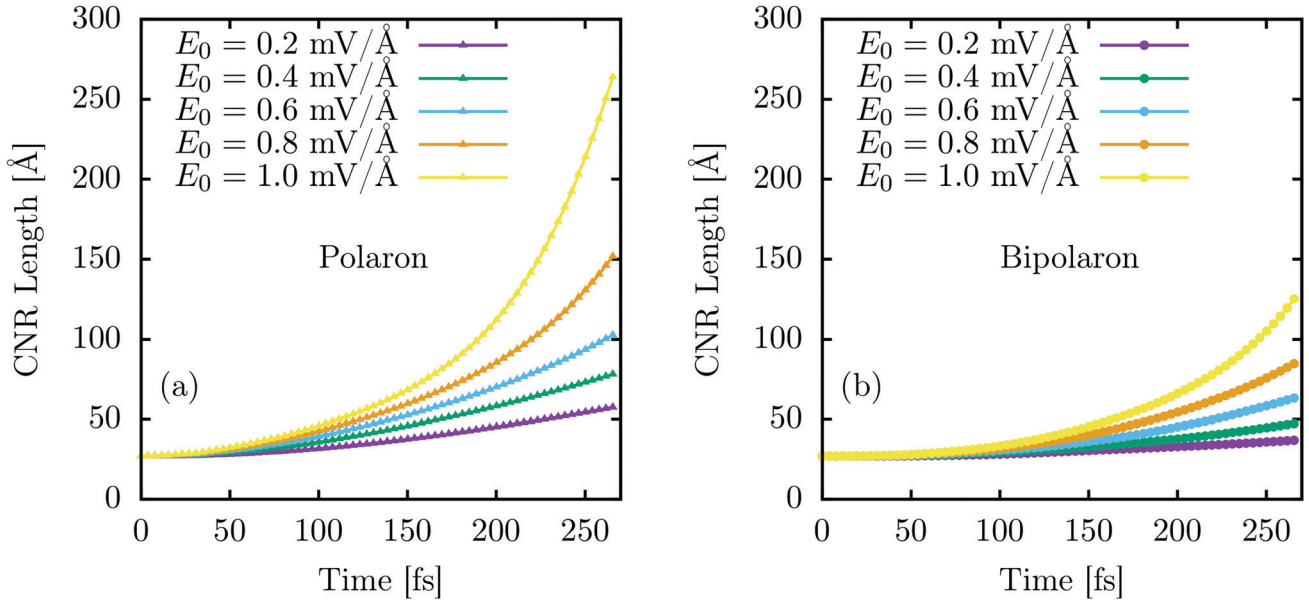

Fig. 5 Time evolution of the charge center (X_{QP}) for (a) a polaron and (b) a bipolaron in ACNR lattices subjected to different electric field strengths.

smaller than the ones reported for the polaron and bipolaron dynamics in standard armchair graphene nanoribbons, which can range within the intervals 2.2–5.1 Å fs^{-1} [28] and 0.15–1.3 Å fs^{-1},[20] respectively, depending on the ribbon's width. Such differences in saturation velocities among these two types of nanoribbons come from the particular transport mechanism present by CNRs. After the movement starts, the carriers perform cell-to-cell hoppings so that the charge density decreases in one cell and increases on the next one subsequently, always involving three coronene cells in the transport mechanism. This process tends to occur slowly once the quasiparticle needs to gain a substantial amount of energy to overcome the potential barrier imposed by the interface between two consecutive coronene cells. In the polaron case, as it gains energy, its speed also increases and its delocalization, which could make it less stable and easy to dissociate in the presence of impurities and lattice defects. In contrast, the bipolaron moves at a slower rate by conserving its localization, being more stable than the polaron over the simulation time. It is worthwhile to mention that in GNRs the charge density is transferred atom-to-atom since these lattices present a constant width along their length. On the other hand, in CNRs, the width changes periodically along the

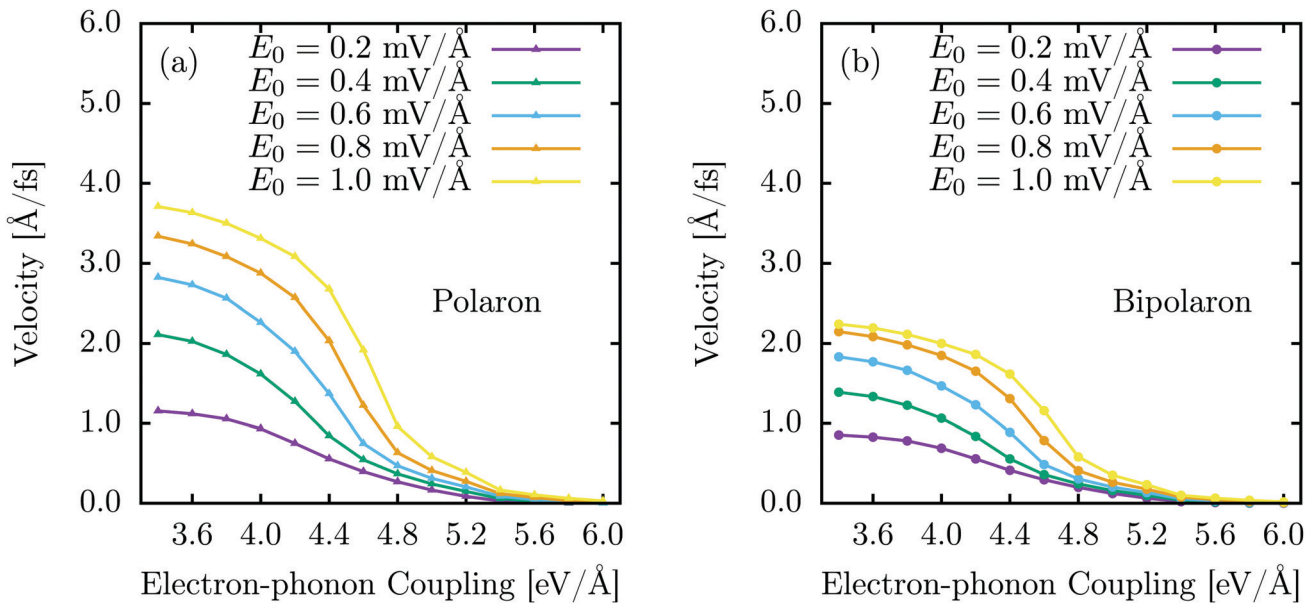

Fig. 6 Saturation velocity as a function of the electron–phonon coupling for (a) a polaron and (b) a bipolaron in ACNR lattices subjected to different electric field strengths.

ribbon's length. In this way, the carriers face discontinuities along the CNR length and they are forced to perform, as mentioned above, cell-to-cell hoppings.

Finally, we complement the discussions about the transport mechanism in CNRs by presenting the dynamics of the charge center X_{QP} for different electric field strengths (Fig. 5) and the interplay between the polaron/bipolaron saturation velocity and electron–phonon coupling strength for some representative electric field regimes (Fig. 6). Fig. 5(a and b) show X_{QP} as a function of time for the polaron and bipolaron cases, respectively. In theses figures one can observe that both the polaron and bipolaron respond to small field strengths (about 0.2 mV Å^{-1}) showing a linear motion. On the other hand, for a high field value (about 1.0 mV Å^{-1}) the charge center moves by showing exponential and quadratic signatures when it comes to polaron and bipolaron cases, respectively. Fig. 6(a and b) show the terminal velocity as a function of electron–phonon coupling strength for the polaron and bipolaron cases, respectively. In both figures, one can note that the terminal velocity decreases when the strength of the electron–phonon coupling increases. After 5.2 eV Å^{-1}, the charge carriers start to present null velocities for the smaller electric field strength considered here. For 6.0 (5.8) eV Å^{-1}, the polaron (bipolaron) presents null velocities regardless of the electric field strength. In these cases, the atomic charge tends to be highly concentrated in a very small part of the lattice. Such a trend for the charge localization increases substantially the local lattice deformations. Since charge and lattice deformations are strongly coupled for electron–phonon coupling regimes above the critical one (5.2 eV Å^{-1}), the effective mass of the quasiparticles increases in a prohibitive fashion to realize their transport.

4 Conclusions

In summary, we have employed a 2D tight-binding Hamiltonian model, which includes lattice relaxation effects, to study the transport of polarons and bipolarons in coronene-like graphene nanoribbons. Based on our approach, the impact of electron–phonon coupling strength on the formation of polarons and bipolarons in nanoribbons with an armchair or zigzag edge was discussed. Our findings have revealed that stable charge carriers can be formed in CNRs with both types of edges. Importantly, zigzag CNRs can represent an advancement for applications in which the generation of polarons and bipolarons plays an important role since these quasiparticles are not formed in standard zigzag graphene nanoribbons. The numerical protocol employed here can accurately determine the bandgap for CNRs according to experimental observations. The bandgap is inferred from the density of states plots and the electron–phonon coupling strength of 5.2 eV Å^{-1} was found as a precise value to reproduce the experimental bandgap. The electron–phonon coupling calculations have also reveled that armchair CNRs are lattices with a lower degree of distortion. Even so, stable polarons and bipolarons can be formed in these lattices. During the transport, it was obtained here that polarons and bipolarons move in the direction of the electric field reaching saturation velocities of 0.38 Å fs^{-1} and 0.19 Å fs^{-1}, respectively. It is important to note that, these velocities are substantially smaller than the ones reported for the polaron dynamics in standard armchair graphene nanoribbons, which can range from 2.2 up to 5.1 Å fs^{-1} depending on the ribbon's width.[28] Such differences in saturation velocities among these two types of nanoribbons come from the particular transport mechanism presented by CNRs, as discussed in the section above. These charge carriers can move only in armchair-like lattices. A polaron is considerably more mobile than a bipolaron, but the former is a less stable quasiparticle. We have obtained that both the polaron and bipolaron respond to small field strengths (about 0.2 mV Å^{-1}) showing a linear motion. For a high field value (about 1.0 mV Å^{-1}) these charge carriers move by showing exponential-like and quadratic signatures, when it comes to polaron and bipolaron cases, respectively. From this perspective, CNRs can serve as an alternative to replace the standard graphene nanoribbons when charge transport applications are considered, and bipolarons will indeed mediate the transport.

Conflicts of interest

There are no conflicts to declare.

Acknowledgements

The authors gratefully acknowledge the financial support from Brazilian Research Councils CNPq, CAPES, and FAPDF and CENAPAD-SP for providing the computational facilities. W. F. G. gratefully acknowledges the financial support from FAP-DF grant 00193.0000248/2019-32. L. A. R. J. and G. M. S. gratefully acknowledge, respectively, the financial support from CNPq grants 302236/2018-0 and 304637/2018-1. R. T. S. J. gratefully acknowledges the financial support from CNPq grant 465741/2014-2, CAPES grants 23038.007604/2014-69 and 88887.144009/2017-00, and FAP-DF grants 0193.001366/2016 and 0193.001365/2016.

References

1 H. Shirakawa, *Angew. Chem., Int. Ed.*, 2001, **40**, 2574–2580.
2 A. J. Heeger, *Angew. Chem., Int. Ed.*, 2001, **40**, 2591–2611.
3 A. G. MacDiarmid, *Angew. Chem., Int. Ed.*, 2001, **40**, 2581–2590.
4 H. Sirringhaus, N. Tessler and R. H. Friend, *Science*, 1998, **280**, 1741–1744.
5 R. H. Friend, R. W. Gymer, A. B. Holmes, J. H. Burroughes, R. N. Marks, C. Taliani, D. D. C. Bradley, D. A. D. Santos, J. L. Brédas, M. Lögdlund and W. R. Salaneck, *Nature*, 1999, **397**, 121–128.
6 G. Wang, F. S. Melkonyan, A. Facchetti and T. J. Marks, *Angew. Chem., Int. Ed.*, 2019, **58**, 4129–4142.
7 J. Hou, O. Inganäs, R. H. Friend and F. Gao, *Nat. Mater.*, 2018, **17**, 119–128.
8 A. N. Enyashin and A. L. Ivanovskii, *Phys. Status Solidi B*, 2011, **248**, 1879–1883.

9 D. J. Appelhans, L. D. Carr and M. T. Lusk, *New J. Phys.*, 2010, **12**, 125006.
10 H. Lu and S.-D. Li, *J. Mater. Chem. C*, 2013, **1**, 3677–3680.
11 U. Rohr, P. Schlichting, A. Böhm, M. Gross, K. Meerholz, C. Bräuchle and K. Müllen, *Angew. Chem., Int. Ed.*, 1998, **37**, 1434–1437.
12 A. V. Talyzin, I. V. Anoshkin, A. V. Krasheninnikov, R. M. Nieminen, A. G. Nasibulin, H. Jiang and E. I. Kauppinen, *Nano Lett.*, 2011, **11**, 4352–4356.
13 M. Fujihara, Y. Miyata, R. Kitaura, Y. Nishimura, C. Camacho, S. Irle, Y. Iizumi, T. Okazaki and H. Shinohara, *J. Phys. Chem. C*, 2012, **116**, 15141–15145.
14 J. L. Bredas and G. B. Street, *Acc. Chem. Res.*, 1985, **18**, 309–315.
15 C. Kuhn, *Phys. Rev. B: Condens. Matter Mater. Phys.*, 1989, **40**, 7776–7787.
16 C. Chen, J. Avila, S. Wang, Y. Wang, M. Mucha-Kruczyński, C. Shen, R. Yang, B. Nosarzewski, T. P. Devereaux, G. Zhang and M. C. Asensio, *Nano Lett.*, 2018, **18**, 1082–1087.
17 Y. Sakai and A. Terai, *J. Phys. Soc. Jpn.*, 2019, **88**, 054718.
18 M. Modarresi, A. Mogulkoc, M. Roknabadi and N. Shahtahmasebi, *Phys. E*, 2015, **66**, 303–308.
19 P. H. de Oliveira Neto and T. Van Voorhis, *Carbon*, 2018, **132**, 352–358.
20 G. G. Silva, L. A. R. Junior, M. L. P. Junior, A. L. de Almeida Fonseca, R. T. de Sousa Júnior and G. M. e Silva, *Sci. Rep.*, 2019, **9**, 2909.
21 B. S. Kandemir, *J. Phys.: Condens. Matter*, 2012, **25**, 025302.
22 L. A. Ribeiro, W. F. da Cunha, A. L. d. A. Fonseca, G. M. e Silva and S. Stafström, *J. Phys. Chem. Lett.*, 2015, **6**, 510–514.
23 L. A. Ribeiro, G. G. Da Silva, R. T. De Sousa, A. L. de Almeida Fonseca, W. F. Da Cunha and G. M. e Silva, *Sci. Rep.*, 2018, **8**, 1914.
24 D. A. Areshkin and B. K. Nikolić, *Phys. Rev. B: Condens. Matter Mater. Phys.*, 2010, **81**, 155450.
25 B. M. Wong, S. H. Ye and G. O'Bryan, *Nanoscale*, 2012, **4**, 1321–1327.
26 G. G. Silva, W. F. da Cunha, R. T. de Sousa Junior, A. L. A. Fonseca, L. A. R. Júnior and G. M. e Silva, *Phys. Chem. Chem. Phys.*, 2018, **20**, 16712–16718.
27 W. F. da Cunha, L. A. Ribeiro, A. L. de Almeida Fonseca, R. Gargano and G. M. e Silva, *Carbon*, 2015, **91**, 171–177.
28 W. F. da Cunha, P. H. Acioli, P. H. de Oliveira Neto, R. Gargano and G. M. e Silva, *J. Phys. Chem. A*, 2016, **120**, 4893–4900.
29 A. L. de Aguiar, A. Saraiva-Souza, Z. Bullard, D. W. Maia, A. G. Souza Filho, E. C. Girão and V. Meunier, *Phys. Chem. Chem. Phys.*, 2014, **16**, 3603–3609.
30 W. P. Su, J. R. Schrieffer and A. J. Heeger, *Phys. Rev. Lett.*, 1979, **42**, 1698–1701.
31 W. P. Su, J. R. Schrieffer and A. J. Heeger, *Phys. Rev. B: Condens. Matter Mater. Phys.*, 1980, **22**, 2099–2111.
32 M. M. Fischer, L. E. de Sousa, L. L. e Castro, L. A. Ribeiro, R. T. de Sousa, G. M. e Silva and P. H. de Oliveira Neto, *Sci. Rep.*, 2019, **9**, 1–8.
33 M. M. Fischer, L. A. R. Junior, W. F. da Cunha, L. E. de Sousa, G. M. e Silva and P. H. de Oliveira Neto, *Carbon*, 2020, **158**, 553–558.
34 Z. Kan, M. Khatun and A. Cancio, *J. Appl. Phys.*, 2019, **125**, 164305.